

# **Influence of element substitutions on poisoning behavior of ZrV<sub>2</sub> alloy: theoretical and experimental investigations**

Shuang Yang<sup>a,b</sup>, Runjie Fang<sup>b,c,d</sup>, Guo Yang<sup>b,\*</sup>, Lijun Lv<sup>b</sup>, Xingbo Han<sup>b,\*</sup>,

Wei Liu<sup>b</sup>, Xiujie He<sup>d,\*</sup>, Pengfei Zhu<sup>a</sup>

<sup>a</sup> School of Mathematics, Physics and Statistics, Shanghai University of Engineering Science, Shanghai 201620, China

<sup>b</sup> Shanghai Institute of Applied Physics, Chinese Academy of Sciences, Shanghai 201800, China

<sup>c</sup> China Nuclear Power Technology Research Institute Co. Ltd., Shenzhen 518000, China

<sup>d</sup> Sino-French Institute of Nuclear Engineering and Technology, Sun Yat-sen University, Zhuhai 519082, Guangdong, China

\* Corresponding authors.

E-mail addresses: [hanxingbo@sinap.ac.cn](mailto:hanxingbo@sinap.ac.cn) (X. Han), [hexiujie@mail.sysu.edu.cn](mailto:hexiujie@mail.sysu.edu.cn) (X. He).

## **Abstract:**

An ZrV<sub>2</sub> alloy is typically susceptible to poisoning by impurity gases, which causes a considerable reduction in the hydrogen-storage properties of the alloy. In this study, the adsorption characteristics of oxygen on ZrV<sub>2</sub> surfaces doped with Hf, Ti, and Pd are investigated, and the influence of oxygen on the hydrogen storage performance of the alloy was discussed. Subsequently, the adsorption energy, bond-length change, density of states, and differential charge density of the alloy before and after doping are analyzed using the first-principles method. The theoretical results show that Ti doping has a limited effect on the adsorption of oxygen atoms on the ZrV<sub>2</sub> surface, whereas Hf doping decreases the adsorption energy of oxygen on the ZrV<sub>2</sub> surface. Oxygen atoms are more difficult to adsorb at most adsorption sites on Pd-containing surfaces, which indicates that Pd has the best anti-poisoning properties, followed by Hf. The analysis of the differential charge density and partial density of states shows that the electron interaction between the oxygen atom and surface atom of the alloys is weakened, and the total energy is reduced after Hf and Pd doping. Based on theoretical calculations, the hydrogen-absorption kinetics of ZrV<sub>2</sub>, Zr<sub>0.9</sub>Hf<sub>0.1</sub>V<sub>2</sub>, and Zr(V<sub>0.9</sub>Pd<sub>0.1</sub>)<sub>2</sub> alloys are studied in a hydrogen–oxygen mixture of 0.5 vol% O<sub>2</sub> at 25°C. The experimental results show that the hydrogen-storage capacities of ZrV<sub>2</sub>, Zr<sub>0.9</sub>Hf<sub>0.1</sub>V<sub>2</sub>, and Zr(V<sub>0.9</sub>Pd<sub>0.1</sub>)<sub>2</sub> decrease to 19%, 69%, and 80% of their original values, respectively. The order of alloy resistance to 0.5 vol% O<sub>2</sub> poisoning is Zr(V<sub>0.9</sub>Pd<sub>0.1</sub>)<sub>2</sub>>Zr<sub>0.9</sub>Hf<sub>0.1</sub>V<sub>2</sub>>ZrV<sub>2</sub>. Pd retains its

original hydrogen absorption performance to a greater extent than undoped surfaces, and it has the strongest resistance to poisoning, which is consistent with previous theoretical calculations.

**Keywords:** Hydrogen storage,  $\text{ZrV}_2$ , First-principles, Poisoning effect

## 1 Introduction

The energy crisis and ongoing environmental challenges have received widespread attention in recent years [1-3], driving the development of the thorium molten-salt reactor nuclear-energy system project [4]. However, LiF and  $\text{BeF}_2$  contained in molten-salt fuel produce the radionuclide tritium ( $^3\text{H}$ ) under neutron irradiation [5]. Tritium is dangerous for humans and nature owing to its special properties; however, it is an important strategic resource and has been chosen as a fusion feedstock for the International Thermonuclear Experimental Reactor program [6][7]. Therefore, developing a scheme for tritium absorption and storage is of great practical significance. Because tritium is a beta-emitting radioactive isotope of hydrogen, the chemical properties of tritium and hydrogen are very similar; therefore, most tritium-storage experiments use hydrogen to simulate tritium. Hydrogen can be stored as a gas, liquid, or solid. Gaseous- and liquid-hydrogen storage are energy-intensive and unsafe. Carbon-based physical-adsorption materials, inorganic porous materials, and metallic hydrogen-storage materials are currently used for solid hydrogen storage [8][9]. Compared to other hydrogen-storage methods, metal hydrogen-storage materials have the advantages of safety, multiple cycles, and mature technology [10][11].  $\text{ZrV}_2$  Laves-phase alloys have been extensively studied as a variety of hydrogen-storage materials because they preserve their maximum theoretical hydrogen-storage capacity (3.01 wt. %) [12][13] and have excellent kinetic properties[14] and ultralow equilibrium pressure (lower than  $10^{-4}$  Pa [15] at room temperature). Therefore,  $\text{ZrV}_2$  is used as an excellent getter material and tritium-absorbing alloy. However, in practical applications, impurity gases such as  $\text{CO}_2$ ,  $\text{O}_2$ ,  $\text{CO}$ , and  $\text{H}_2\text{O}$  react with metal on the surface of the alloy to form a dense passivation layer, which decreases the rate of hydrogen absorption [16][18][19]. Therefore, improving the anti-poisoning properties of the  $\text{ZrV}_2$  alloy is important for their widespread application.

In recent decades, many studies have investigated the effects of impurity gases on hydrogen-storage alloys. For example, Zhang et al. [17] studied the poisoning behavior of  $\text{Zr}_{0.8}\text{Ti}_{0.5}\text{V}_{1.7}$  alloy. The 0.1 mol% air impurities in hydrogen only worsened the hydrogen-absorption kinetics at 25 °C, and the 1 mol% air impurities also affected the maximum hydrogen-absorption content at 180 °C. Sun et al. [18] indicated that the hydrogen capacity of the  $(\text{Mg}(\text{NH}_2)_2+2\text{LiH})$  system gradually declined in  $\text{H}_2$  containing 0.1 mol%  $\text{O}_2$ , and it could not be restored to its initial level when using purified hydrogen again. In this poisoning phenomenon, the impurity gas reacts with the alloy surface to prevent hydrogen absorption. Many efforts have been made to protect hydrogen-storage alloys from poisoning. Zhang et al. deposited a layer of Pd-Ag film on the surfaces of  $\text{Zr}_{0.9}\text{Ti}_{0.1}\text{V}_2$ ,  $\text{Zr}_{57}\text{V}_{36}\text{Fe}_7$ , and  $\text{ZrV}_2$ , and the results showed that Pd-Ag could withstand the poisoning effect of air impurities [19]. The hybridizing kinetic properties of all Pd-coated alloys were improved compared to those of the bare alloy [20]. However, the Pd film itself exhibited hydrogen-embrittlement properties. Moreover, the process of hydrogen absorption and desorption for the substrate alloy inevitably led to volume expansion and pulverization, thereby resulting in the disintegration and detachment of the Pd film [19][21]. Therefore, achieving long-term protection was difficult over multiple hydrogen absorption/desorption cycles. Wu et al. [22] explored the poisoning behavior of  $\text{O}_2$  as an impurity in a ZrVNi Laves-phase alloy. They observed that Ni provided surface active sites for the dissociative adsorption of hydrogen molecules during Zr and V oxidation. Significant progress has been made in the study of impurity gas poisoning in hydrogen-storage alloys. However, few theoretical studies have been conducted on the microscopic mechanism of impurity gas poisoning on  $\text{ZrV}_2$  alloy surfaces.

In the present study, first-principles calculations are used to investigate how oxygen atoms occupy adsorption sites on the surfaces of Zr-V-M (M=Hf, Pd, Ti) alloys. The interaction between oxygen and surface atoms is analyzed, and the hydrogen-absorption properties of Zr-V-M (M=Hf, Pd) alloys against gaseous impurities are verified experimentally.

## 2 Models and computational details

First-principles calculations were performed based on density functional theory in the plane-wave pseudopotential approach using the Vienna ab-initio simulation package [23][24]. The exchange-correlation energy was selected based on the general gradient approximation and Perdew–Burke–Ernzerh exchange-correlation potential [25]. The Brillouin zone was sampled using Monkhorst–Pack k-point meshes [26], and a projector-augmented wave was used to generate the pseudo-potential file.  $\text{ZrV}_2$  was selected based on the database [27]; the space group was  $\text{Fd}\bar{3}\text{m}(227)$ ,  $a=b=c=7.36 \text{ \AA}$ , and the unit cell volume was  $398.74 \text{ \AA}^3$ . Based on the calculated  $\text{ZrV}_2$  crystal structure, Zr was substituted with Hf and Ti, and V was substituted with Pd. The corresponding doped alloy model was obtained, as shown in Fig. 1, and geometric optimization was performed. Based on the calculated crystal structure, a seven-layer slab  $\text{ZrV}_2$  surface model was built, separated by a  $15 \text{ \AA}$  vacuum layer, and the lower four layers of the surface were fixed. According to a previous study, the following low-index stoichiometric specific surfaces were selected for cutting from a geometrically optimized block: (1) the Zr terminal of the  $\text{ZrV}_2(100)$  surface and (2) the V terminal of the  $\text{ZrV}_2(100)$  surface. The k-point meshes were  $(12 \times 12 \times 12)$  and  $(5 \times 5 \times 5)$  for the bulk and surface models, respectively. Unit-cell parameters and ion relaxation were allowed during optimization. Based on the convergence tests, the energy cut-off was set to  $520 \text{ eV}$ , the energy convergence standard was  $10^{-5} \text{ eV}$ , and the force convergence standard was  $0.02 \text{ eV/\AA}$ .

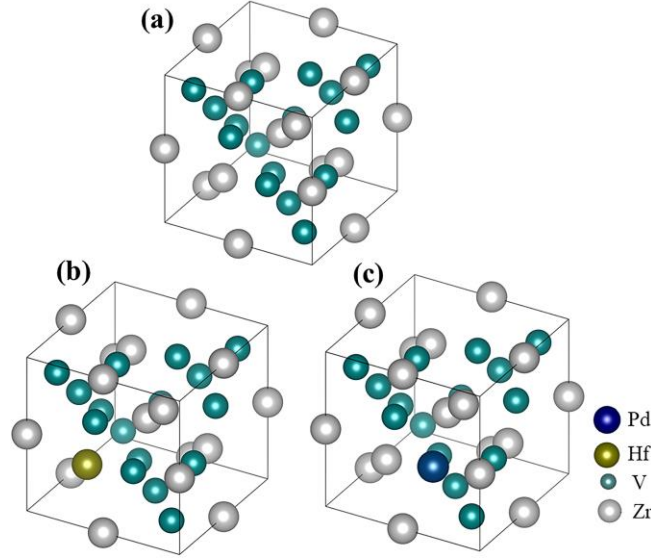


**Fig. 1** Schematic of the bulk phase model of the Zr-V-M system: (a) ZrV<sub>2</sub>, (b) A-side substitution (ZrVHf), (c) B-side substitution (ZrVPd)

For the optimization results, taking ZrV<sub>2</sub> as an example, the surface energy used to compare the stability of each low-exponential surface is defined as [28]:

$$\gamma_s = \frac{1}{2A} [E_{slab} - NE_{bulk}] \quad (1)$$

where  $\gamma_s$  (J/m<sup>2</sup>) is the surface energy,  $E_{slab}$  (eV) is the total energy of the optimization,  $A$  (Å<sup>2</sup>) is the surface area,  $N$  is the number of atoms corresponding to the element in the surface model and  $E_{bulk}$  is the total energy of the bulk phase ZrV<sub>2</sub>.

The change in surface energy before and after doping is used to reflect the degree of stability of the doped surface. The doping energy is defined as:

$$E_d = E_{ZrV_2}^{substituted} - E_{ZrV_2}^{slab} - \sum_i \Delta N_i E_i \quad (2)$$

where  $E_{ZrV_2}^{substituted}$  is the energy of the doped surface model,  $\Delta N_i$  is the increase or decrease in a component (e.g., as the A site is replaced, the Zr atom decreases, and the dopant atom increases), and the  $E_i$  is the corresponding block energy of the component.

Based on the surface-optimization results, the surface with the lowest energy (the most stable surface) was selected for the subsequent study of adsorption behavior. The surface of ZrV<sub>2</sub> included many O atomic adsorption sites. For the Zr terminal of the ZrV<sub>2</sub>(100) surface ((100)-Zr), there are four highly symmetrical adsorption sites: top,

bridge, hollow3, and hollow4. For the V terminal of the  $\text{ZrV}_2(100)$  surface (defined as (100)-V), there are two bridge sites (defined as bridge1 and bridge2) and two top sites (defined as top1 and top2), as shown in Fig. 2. Adsorption energies are calculated as follows:

$$E_{ads} = E_{slab + adsorbate} - E_{slab} - E_{adsorbate} \quad (3)$$

where  $E_{ads}$  is the adsorption energy, and  $E_{slab + adsorbate}$ ,  $E_{slab}$ , and  $E_{adsorbate}$  are the energies of oxygen on the  $\text{ZrV}_2(100)$  surface,  $\text{ZrV}_2(100)$  surface, and adsorbed oxygen, respectively.

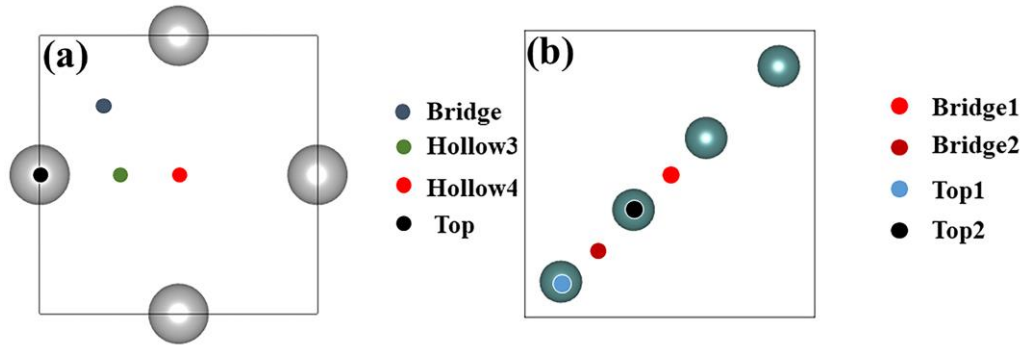


**Fig. 2** Surface adsorption sites of  $\text{ZrV}_2$ : (a) Zr-(100), (b) V-(100)

The differential charge density reflects the flow of electrons before and after the formation of the surface structure, which is the difference between the space charge densities before and after bonding. In this study, the differential charge is defined as:

$$\Delta\rho = \rho_{AB} - \rho_A - \rho_B \quad (4)$$

where  $\rho_{AB}$  represents the surface after oxygen adsorption,  $\rho_A$  represents the unabsorbed pure surface, and  $\rho_B$  represents the adsorbed atoms.

### 3 Experimental proedure

#### 3.1 Material preparation

The Zr-V-doped alloy was prepared using vacuum arc melting at the following composition ratios:  $\text{ZrV}_2$ ,  $\text{ZrV}_{1.8}\text{Pd}_{0.2}$ , and  $\text{Zr}_{0.9}\text{Hf}_{0.1}\text{V}_2$ . The purity of the raw alloy exceeded 99.9%. The alloy was placed in a DHL-400 arc-melting furnace (Shenyang Scientific Instrument Co., Ltd., Chinese Academy of Sciences, China). Each ingot was remelted seven times under the protection of purified argon gas. The alloy ingots were furnace-cooled to  $25^\circ\text{C}$  to obtain the as-cast ingots. To obtain an alloy with a uniform

phase structure, the vacuum-encapsulated sample was heated to 1273 K for 168 h in a muffle furnace and then cooled to room temperature to obtain an annealed alloy.

### 3.2 Structure characterization

The alloy phase compositions and cell parameters were determined using an X-ray diffractometer. The X-ray patterns were collected between diffraction angles of  $10^{\circ}$ – $90^{\circ}$  ( $2\theta$ ) with a step-scanning mode (step width 0.03, counting time 0.5 s). The phase distribution was observed using a scanning electron microscope (LEO 1530vp) in the backscattering electron imaging mode.

### 3.3 Hydrogen-absorption kinetics of poisoned alloy

In this study, the experiment on the poisoning of  $\text{ZrV}_2$ ,  $\text{ZrV}_{1.8}\text{Pd}_{0.2}$ , and  $\text{Zr}_{0.9}\text{Hf}_{0.1}\text{V}_2$  alloys was carried out on a comprehensive test device designed and constructed in the laboratory for low-pressure hydrogen-storage performance. The amount of hydrogen absorbed by the alloy was determined using the volume method [29]. First, approximately 1 g of bulk sample was selected for testing, and the oxide layer on the surface of the samples was sanded with 300 mesh sandpaper. Before testing, each sample was activated by heating the sample chamber to 500 °C and pumping the chamber for 2 h. Then, the samples were cooled to 350 °C to continue the activation process. The hydrogen absorption process was repeated until the kinetic curves coincided, which indicated that the samples were fully activated. Fully activated samples were exposed to a hydrogen–oxygen mixture containing 0.5 vol%  $\text{O}_2$  at room temperature. The pressure decrease was measured as a function of time and translated into hydrogen absorption capacity, which was expressed as a weight percentage (wt. %H).

## 4 Results and discussion

### 4.1 Oxygen-absorption behavior

The two low-index surfaces of  $\text{ZrV}_2$  were optimized. According to Eq (1), the surface energy of (100)-Zr is 2.11 J/m<sup>2</sup>, and the surface energy of (100)-V is 2.11 J/m<sup>2</sup>; the two low-index surfaces of  $\text{ZrV}_2$  are shown in Fig. 3. The surface energies are similar, which indicates that the different cutoff surfaces do not significantly affect the surface stability. In view of the above results, there are several changes in the surface model of

element doping. First, the doping element replaces the A or B sites. Second, the relative position of the substituted element in the 100-V and 100-Zr planes should position the doping atoms as close to the outermost layer as possible. Table 1 lists the only few stable patterns after optimization in all combinations (Fig. 4): for the first layer of the Zr terminal of the  $\text{ZrV}_2(100)$  surface model, Hf is used instead of Zr (defined as  $\text{ZrVHf-100Zr1-A}$ ); for the first layer of the V terminal of the  $\text{ZrV}_2(100)$  surface model, Pd is used instead of V (defined as  $\text{ZrVPd-100V1-B}$ ), and for the first layer of the Zr terminal of the  $\text{ZrV}_2(100)$  surface model, Ti is used instead of Zr (defined as  $\text{ZrVTi-100Zr1-A}$ ).

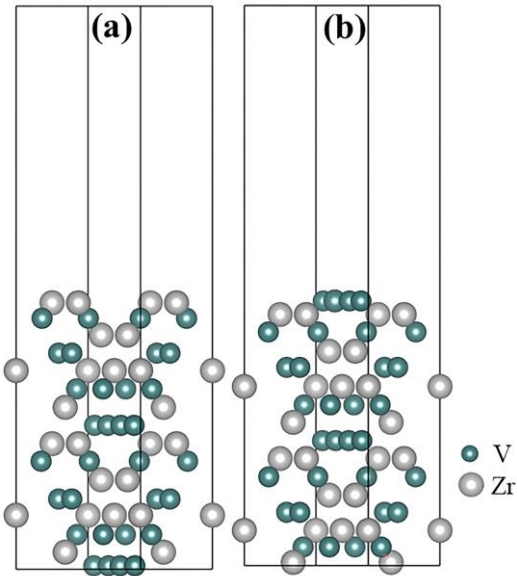


**Fig. 3** Two low-index surfaces of  $\text{ZrV}_2$ : (a) the (100)-Zr model, (b) the (100)-Zr model

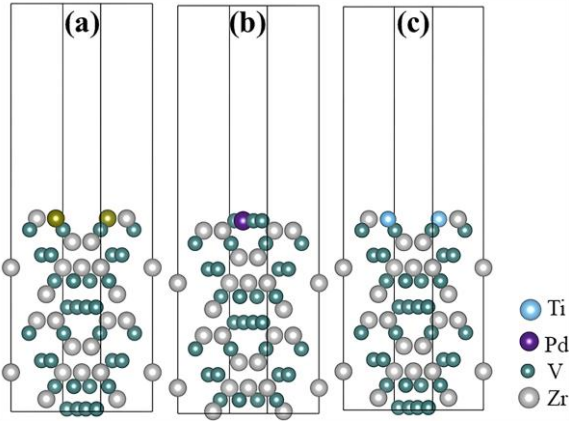


**Fig. 4** Several doped surface models for the stable presence of: (a)  $\text{ZrVHf-100Zr1-A}$ , (b)  $\text{ZrVPd-100V1-B}$ , (c)  $\text{ZrVTi-100Zr1-A}$

**Table 1** Surface energy and doping energy for each type of doped surface

Surface type	Surface energy $\gamma_s$ (J/m <sup>2</sup> )	Doping energy $E_s$ (eV)
ZrVHf-100Zr1-A	2.37	-0.70
ZrVPd-100V1-B	1.94	-0.95
ZrVTi-100Zr1-A	2.02	-0.58

The results show that the doping energies of ZrVPd-100V1-B, ZrVTi-100Zr1-A, and ZrVHf-100Zr1-A are negative. The energy of the system decreases owing to doping, which indicates that the formation of these three structures is most likely. Pd, Ti, and Hf tend to segregate at the surface, which may affect the anti-poisoning.

Based on the surface-optimization results, the adsorption behaviors of the most likely formed Ti, Hf, and Pd surfaces are studied. First, the possible adsorption configurations are clarified. The adsorption energies of each highly symmetrical adsorption site on the Zr and V terminals of the ZrV<sub>2</sub>(100) surface are listed in Table 2. Among the various sites, the hollow4 site on (100)-Zr is the unstable adsorption site, whereas the bridge site on (100)-Zr and bridge2 site on (100)-V are the most stable adsorption sites on the surface. Therefore, oxygen atoms on the surface of the poisoned alloy tend to be adsorbed at these two sites; thus, they are selected as reference sites for the change in adsorption energy before and after doping.

**Table 2** Adsorption energy of oxygen atoms at different sites on different surfaces of ZrV<sub>2</sub>

(100) -Zr		(100) -V	
Adsorption site	Adsorption energy (eV)	Adsorption site	Adsorption energy (eV)
top	-6.22	top1	-8.60
<b>bridge</b>	<b>-8.56</b>	top2	-7.14
hollow3	1.61	bridge1	-7.90
hollow4	8.26	<b>bridge2</b>	<b>-8.68</b>

Table 3 shows that when Ti is doped on the ZrV<sub>2</sub> surface, the adsorption energy of oxygen atom changes from -8.68 eV to -7.7 eV. Therefore, Ti has almost no inhibitory effect on the adsorption energy of the oxygen atoms. When Hf is doped on the surface of ZrV<sub>2</sub>, the adsorption energy of the oxygen atom changes from -8.56 eV to -1.1 eV, and the oxygen atoms cannot be adsorbed on the surface after Pd doping. In particular,

the Pd atom located in the first layer of (100)-V destroys one of the two bridge2 adsorption sites close to the atom; thus, the oxygen atoms can no longer be combined. The oxygen atoms can only be adsorbed at the bridge2 site or the more unstable top site, thereby significantly weakening the maximum oxygen coverage and average oxygen atom binding energy.

**Table 3** The most stable oxygen atom adsorption energy for each doped surface

Surface types	Adsorption energy (eV)	Adsorption energy difference before and after adsorption (eV)
ZrVHf-100Zr1-A	-1.10	7.46
ZrVPd-100V1-B	Unable adsorbed	/
ZrVTi-100Zr1-A	-7.70	0.86

The effect of Pd on each adsorption site is studied for the Pd-doped group that exhibits the best anti-poisoning potential. The ZrVPd-100V1-B type surface lost its original symmetry owing to the emergence of Pd, thereby resulting in new adsorption sites (Fig. 5). Table 4 lists the adsorption status of all sites on the Pd-doped surface. The results show that Pd biasing to the first layer of the V-terminal of the  $\text{ZrV}_2(100)$  surface cancels or weakens the adsorption stability of most bridge sites. This forces oxygen atoms to migrate to the more unstable top sites, thereby indicating that Pd has superior anti-poisoning properties.

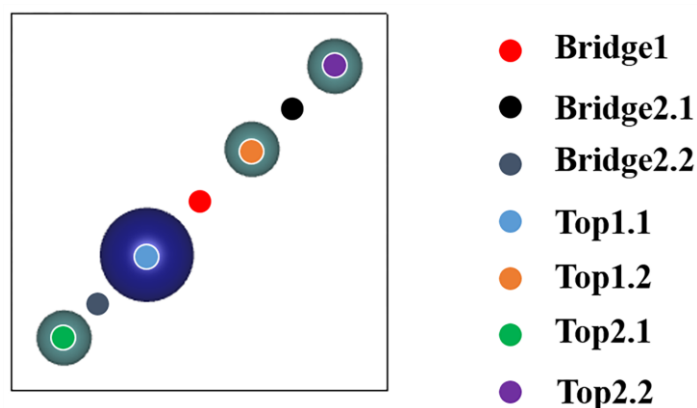


**Fig. 5** Adsorption sites on the ZrVPd-100V1-B surface

**Table 4** Oxygen atom adsorption energy at each site on the two doped surfaces of Pd

ZrVPd-100V1-B	top1.1	top1.2	top2.1	top2.2	bridge1	bridge2.1	bridge2.2
Adsorption energy (eV)	/	-3.70	-7.14	-7.16	-3.94	/	/
Adsorption energy increments (eV)	/	4.90	0.00	-0.02	3.96	/	/

The effects of adsorption and doping on the bond length of the system are studied. First, bridge-site adsorption is investigated on two low-index undoped surfaces. Fig. 6(a) and (b) show the O atoms adsorbed on the  $\text{ZrV}_2(100)$  surface. The adsorbed O atoms (marked by red spheres) have a clear tendency to approach the V atoms to form strong bonds. Even for the Zr terminal of the  $\text{ZrV}_2(100)$  surface, V atoms are located in the second layer and attract surface oxygen atoms to the interior to form bonds with them. It can be inferred that the V atom has better oxygen affinity than that of Zr. Second, for the case of Ti and Hf (A-site) doping, Fig. 6(c)(d) shows that the O-V distance elongates from 2.0 Å to 3.0 Å for Ti doping and from 2.0 Å to 3.33 Å for Hf doping. Compared with those of Ti, the offset of the oxygen atom is more pronounced, and the lattice distortion is greater under Hf doping, which breaks the high-symmetry binding site of the O atom and forces it to shift to a more unstable position. Finally, for the case of Pd (B-site) doping, Fig. 6(e) shows that the O-V distance is 1.88 Å before doping and 2.12 Å after doping, which indicates that the O atom is weakly adsorbed and easily desorbed under external influence.

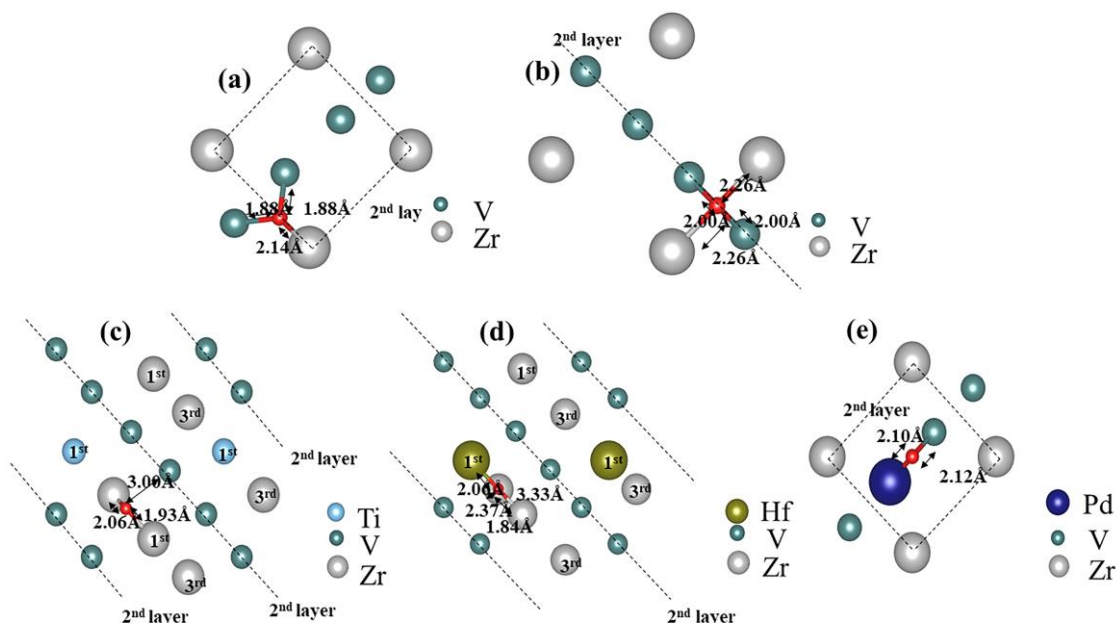


**Fig. 6** Several oxygen adsorption optimized pristine-surface structures: (a) Bridge site of 100-Zr, (b) Bridge1 site of 100-V, (c) Bridge site of ZrVTi-100Zr1-A, (d) Bridge site ZrVHf-100Zr1-A, (e) Bridge1 site ZrVPd-100V1-B

## 4.2 Differential charge density and density of states

In the previous section, the ZrVHf and ZrVPd alloys were determined to have the best anti-poisoning effects by analyzing the adsorption behavior of oxygen atoms. Gaining a deep understanding of O adsorption on ZrVHf and ZrVPd alloy surfaces is necessary from an atomic point of view. Therefore, the differential charge density and density of states (DOS) were calculated.

The DOS and differential charge density can help us better understand the bonding characteristics between atoms and the difficulty of electron gain and loss between O atoms and doped surface structures. Therefore, the DOS and differential charge densities are analyzed to more accurately understand the interaction mechanism between O atoms and surfaces. Fig. 7 shows the charge transfer at the Zr/V terminal of the ZrV<sub>2</sub>(100) surface and the corresponding modified surface before and after adsorption. The green area in the figure indicates charge loss before relative adsorption, whereas the red area indicates charge before relative adsorption. After oxygen adsorption, oxygen atoms tend to gain electrons, and the overlap of electron clouds and electron gain/loss between V-O is more evident than that of Zr-O. Stronger covalent

bonds can be formed between V-O, and the bond lengths are shorter compared to those of Zr-O. After elemental substitution, gaps appeared in both the gain and loss electron structures of the doped surface compared to those of the original surface. The decreased ability of doped atoms to lose electrons as well as smaller oxygen atom interactions lead to a decrease in oxygen atom binding.

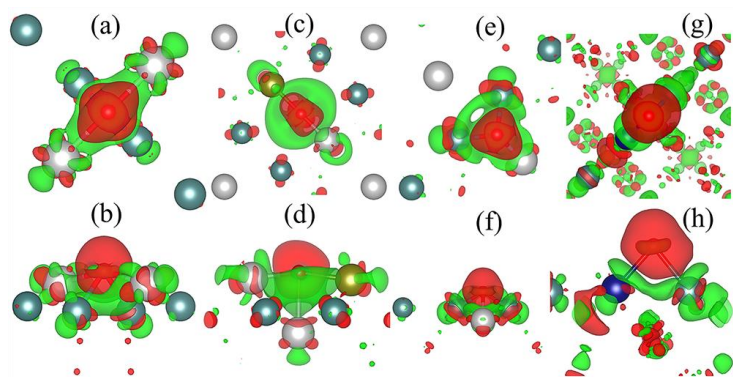


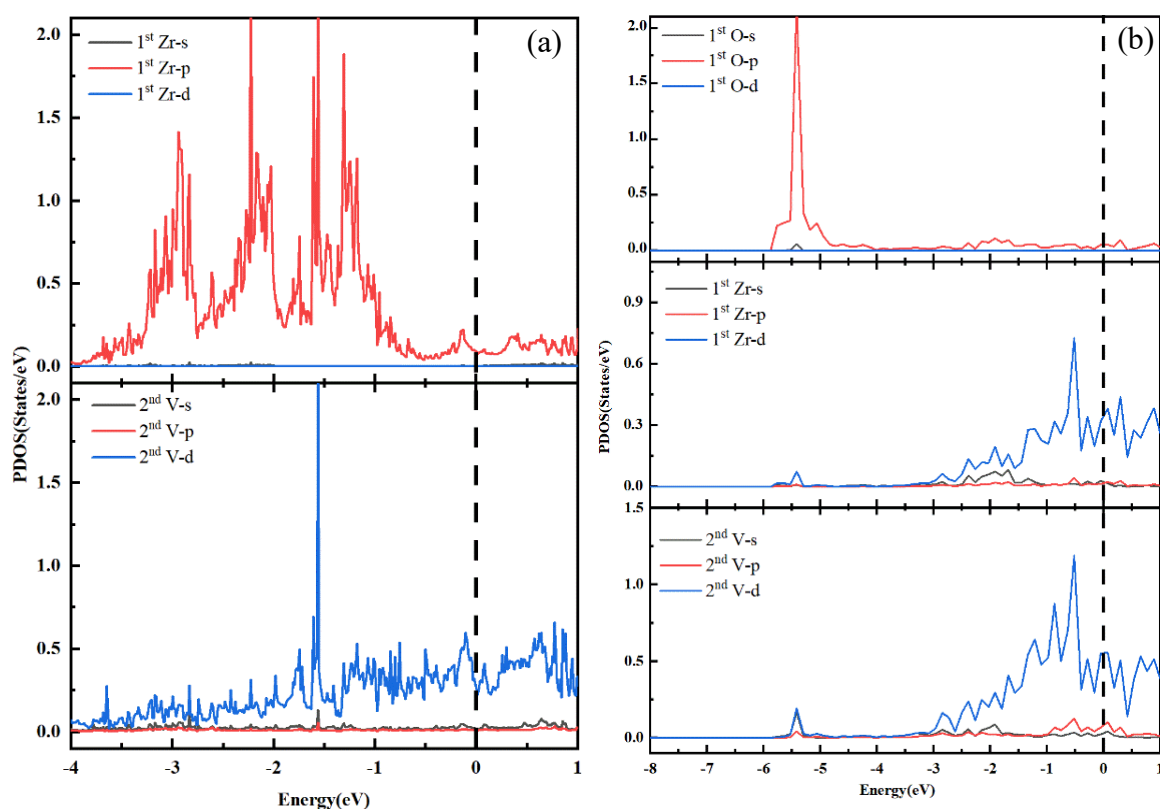
**Fig. 7** Differential charge density diagrams for each surface: (a) top view of Zr terminal of  $\text{ZrV}_2(100)$  surface model; (b) side view of Zr terminal of  $\text{ZrV}_2(100)$  surface model; (c) top view of Hf-doped  $\text{ZrV}_2(100)$  surface model; (d) side view of Hf-doped  $\text{ZrV}_2(100)$  surface model; (e) top view of V terminal of  $\text{ZrV}_2(100)$  surface model; (f) side view of V terminal of  $\text{ZrV}_2(100)$  surface model; (g) top view of Pd-doped  $\text{ZrV}_2(100)$  surface model; (h) side view of V-doped  $\text{ZrV}_2(100)$  surface model

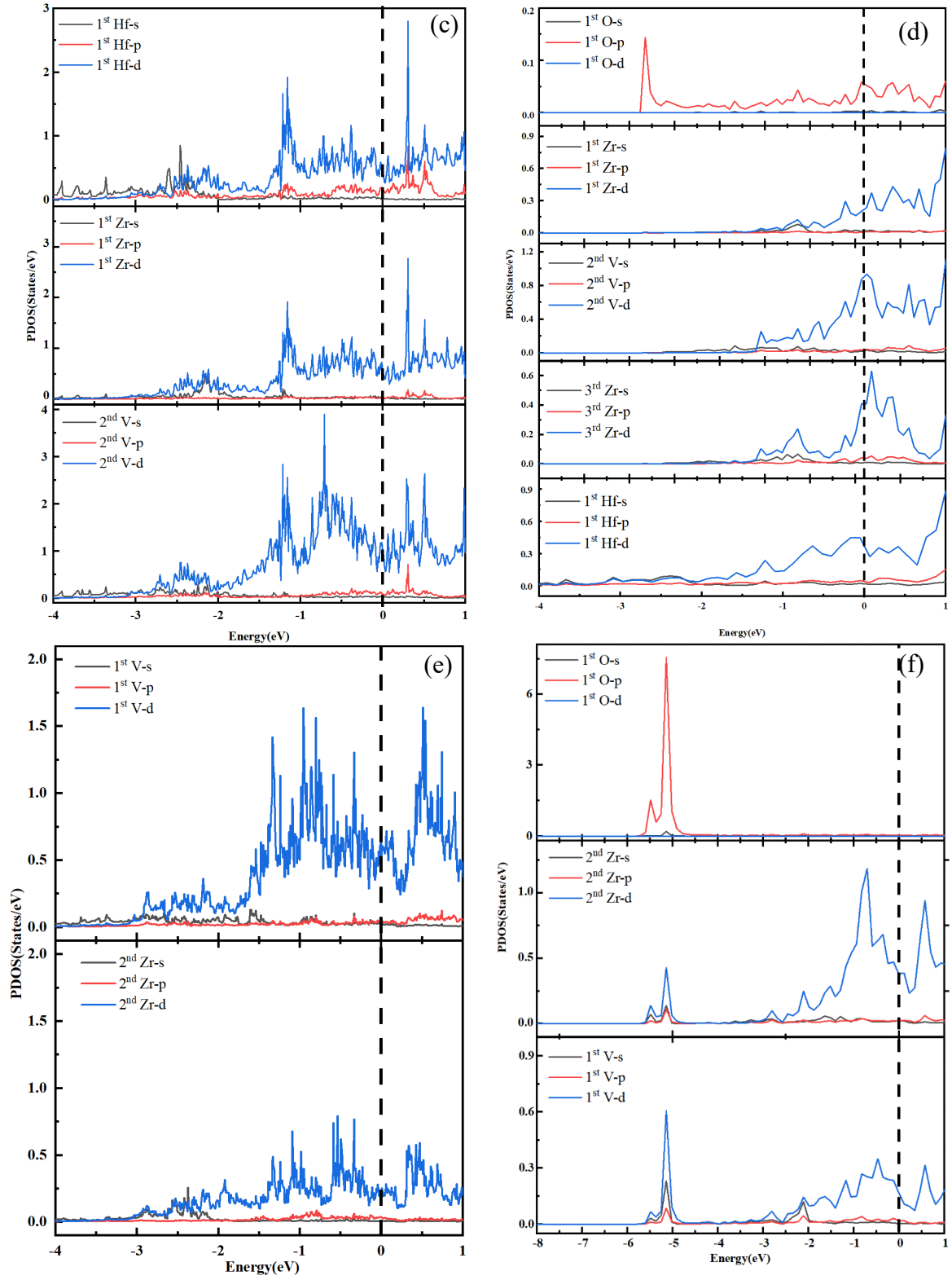
The DOS is a key parameter for studying atomic bonding and material properties [30]. The bonding properties can be clearly described by the energy-level distribution of the electrons. As shown in Fig. 8, the Fermi-energy level is automatically normalized to 0 eV using the software and is marked with a dotted line in the figure. For the Zr terminal of the  $\text{ZrV}_2(100)$  surface in Fig. 8 (a), a strong orbital hybridization can be observed between the p orbital of the Zr atom in the first layer and the d orbital of the V atom in the second layer at approximately -1.6 eV. After the A-site substitution by Hf in Fig. 8 (c), the interaction between Zr and V weakens. The Hf atom p orbital hybridizes with the Zr and V atom d orbital at -1.1 eV. When an O atom is adsorbed on the Hf-doped surface, the electron energy decreases (-3 eV to 0 eV). The interaction between the O atom and surface atoms disappears; thus, chemisorption changes to physical adsorption. The presence of Hf destroys the stable adsorption sites of the O

atoms owing to the obvious distortion of the surface structure after adsorption.

The electron energy-distribution pattern is different for the V terminal of the  $\text{ZrV}_2(100)$  surface. There is an orbital hybridization between the V atom s orbital in the first layer and the Zr atom p orbital in the second layer in the range of -1.5 eV and -1 eV, which is minimized after Pd doping.

According to the above analysis, almost no hybridization orbitals exist between the doped surface atoms and oxygen atoms, which also indicates that doping with Hf and Pd weakens the adsorption effect of O.





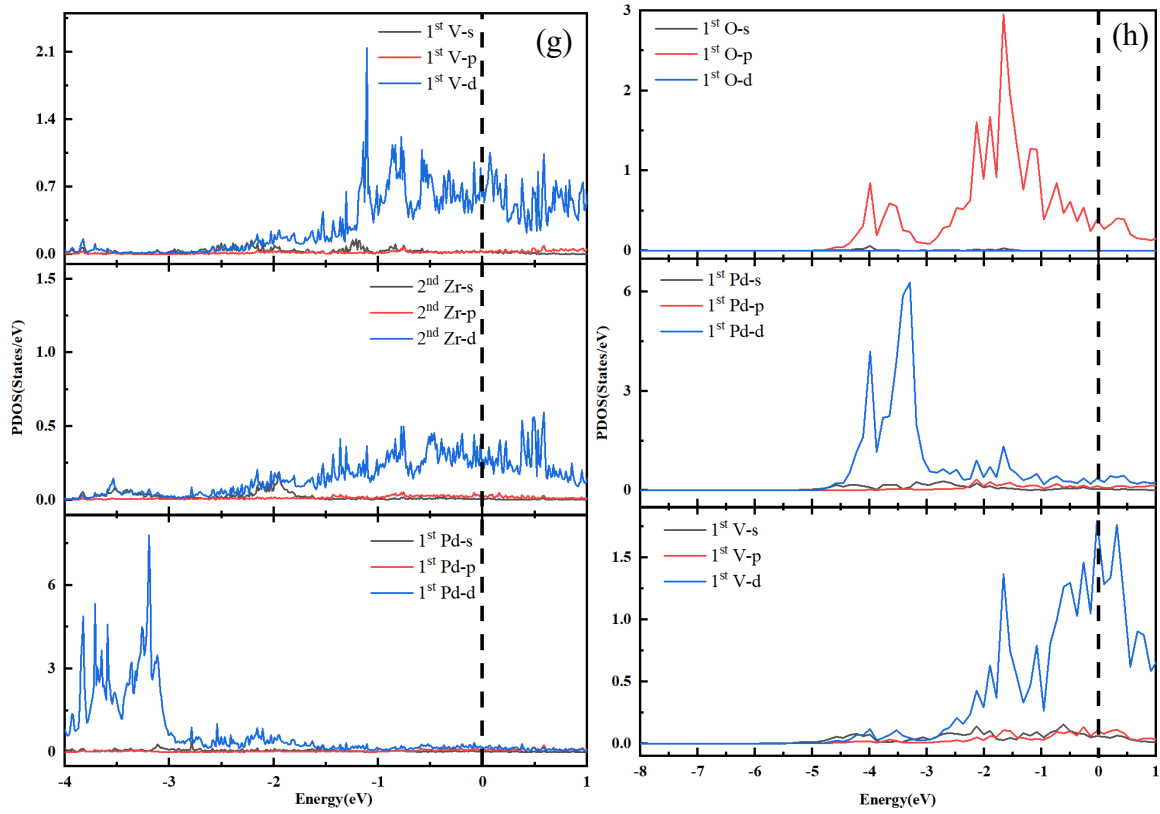


**Fig. 8** Partial density of states (PDOS) profiles for each surface: (a) Zr terminal of  $\text{ZrV}_2(100)$  surface; (b) Zr terminal of  $\text{ZrV}_2(100)$  surface after oxygen atom adsorption at the bridge site; (c)  $\text{ZrVHf-100Zr1-A}$ ; (d)  $\text{ZrVHf-100Zr1-A}$  after oxygen atom adsorption at the bridge site; (e) V terminal of  $\text{ZrV}_2(100)$  surface; (f) V terminal of  $\text{ZrV}_2(100)$  surface after oxygen atom adsorption at the bridge site; (g)  $\text{ZrVPd-100V1-B}$ ; (h)  $\text{ZrVPd-100V1-B}$  after oxygen atom adsorption at the bridge site

### 4.3 Phase composition and microstructure

After the homogenization annealing treatment, the Zr-V-M (M=Hf, Pd) series alloys are characterized using X-ray diffractometer and scanning electron microscope. The XRD results are shown in Fig. 9. All alloys are primarily composed of  $\text{ZrV}_2$  and  $\text{Zr}_3\text{V}_3\text{O}$  phases. The  $\text{Zr}_3\text{V}_3\text{O}$  phase is owing to the marginal oxidation of the raw material during the annealing treatment, which is similar to the results of previous studies [31][33]. The addition of Hf does not introduce a new phase into the alloy but forms a solid solution. However, a particular amount of  $\text{Zr}_2\text{Pd}$  and  $\text{Pd}_3\text{V}$  phases are observed in the Pd-containing samples. This is determined by the poor solid-solution properties of the Zr-Pd-V system itself, which is consistent with previous reports [34].

The difference in the XRD results is mainly related to the solubility of the doped elements relative to Zr or V. Hf can combine with V over a wide range to form  $\text{HfV}_2$  belonging to the C15 Laves phase, which remains in the  $\text{ZrV}_2$  lattice without precipitation. Pd combines with Zr and V to form  $\text{PdV}_3$  with a Pm-3m structure and  $\text{Zr}_2\text{Pd}$  with an I4/mmm structure, respectively, which are not miscible with  $\text{ZrV}_2$ . No solidification bias phases were visible in the three alloy samples owing to the doping. The samples are not brought into phase with the C14 or C36 Laves phases, thereby indicating good phase uniformity. Fig. 10 shows the SEM backscattering electron images of the Zr-V-M (M=Hf, Pd) series of alloys. Based on the principle of backscattering imaging, the dark gray areas correspond to the  $\text{ZrV}_2$  phase, the white areas to the Zr phase, and the small black areas to the V phase. The energy dispersive spectrometer mapping of the Zr-V-M (M=Hf, Pd) series of alloys is shown in Fig. 11. The results illustrate that Zr, V, Hf, and Pd are uniformly distributed in the selected region of the alloy sample. The characterization results of the four groups of gold showed that the 1000 °C vacuum heat treatment considerably improved the homogeneity of the alloy, the second phase segregation was weakened, and the doped elements were well solidified with the matrix.

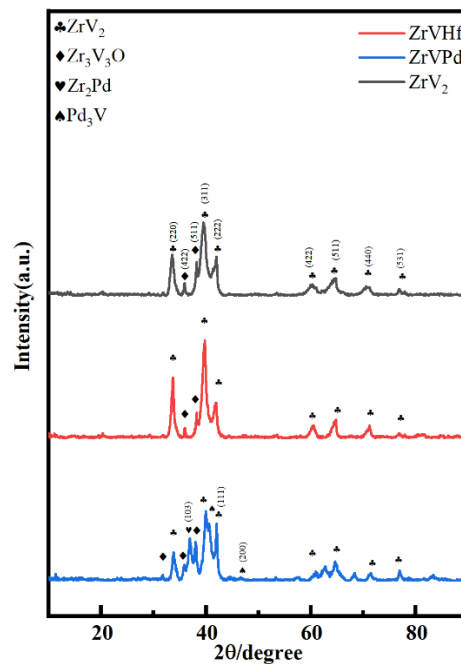


**Fig. 9** XRD pattern of Zr-V-M (M=Hf, Pd) system alloys

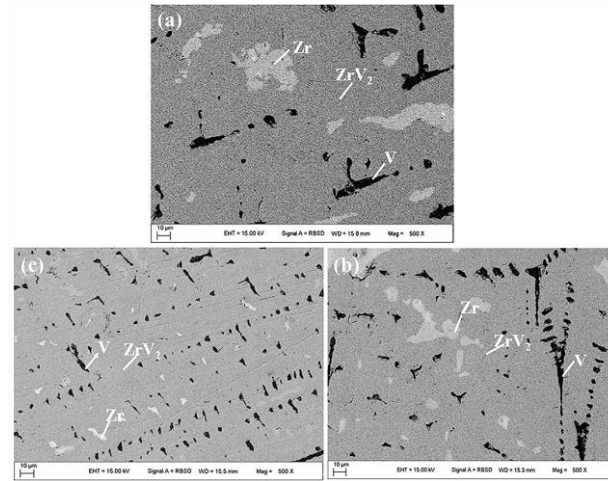


**Fig. 10** SEM backscattering electron images of Zr-V-M (M = Hf, Pd) alloys: (a)  $\text{ZrV}_2$  alloy, (b)  $\text{ZrV}_{1.8}\text{Pd}_{0.2}$  alloy, (c)  $\text{Zr}_{0.9}\text{Hf}_{0.1}\text{V}_2$  alloy

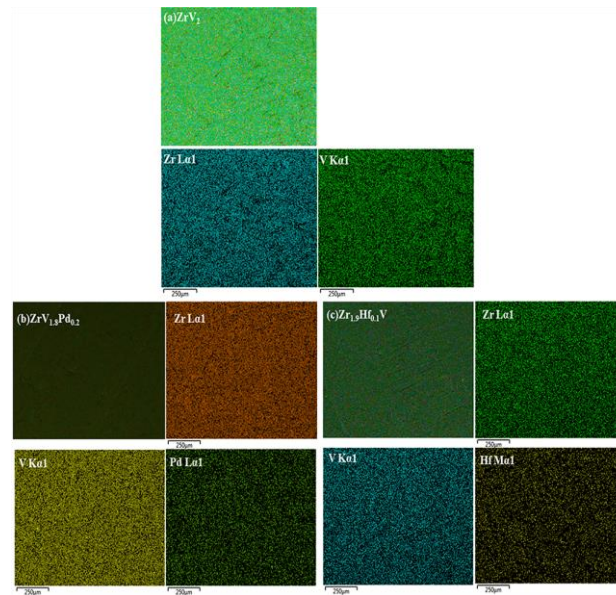


**Fig. 11** EDS mapping of Zr-V-M (M = Hf, Pd) alloys: (a)  $\text{ZrV}_2$  alloy, (b)  $\text{ZrV}_{1.8}\text{Pd}_{0.2}$  alloy, (c)  $\text{Zr}_{0.9}\text{Hf}_{0.1}\text{V}_2$  alloy

#### 4.4 Hydrogenation properties of the poisoned Zr-V-M (M=Hf, Pd) alloy

Zhang et al. [16] showed that the hydrogen-absorption ability of  $\text{Zr}_{0.9}\text{Ti}_{0.1}\text{V}_2$  alloy is minimized when exposed to oxygen, and after regeneration, the oxygen-poisoned  $\text{Zr}_{0.9}\text{Ti}_{0.1}\text{V}_2$  sample hardly absorbs hydrogen. Therefore, the main simulation results are confirmed by studying the hydrogen-absorption kinetic behaviors of  $\text{ZrV}_2$ ,  $\text{Zr}_{0.9}\text{Hf}_{0.1}\text{V}_2$ , and  $\text{ZrV}_{1.8}\text{Pd}_{0.2}$  alloys in a hydroxide mixture of 0.5 vol%  $\text{O}_2$  at room temperature. Fig. 12 shows the kinetic curves of the two doped alloys and the  $\text{ZrV}_2$  alloy at room temperature. The vertical axis of the curve represents the ratio of the hydrogen

absorption  $H/M$  to the last pure hydrogen absorption  $H/M$  before the poisoning. The degree of depreciation in the amount of hydrogen stored after poisoning is different in the three cases:  $ZrV_2$  retained 19% of the original amount,  $Zr_{0.9}Hf_{0.1}V_2$  retained only 69% of the original amount of hydrogen absorbed, and  $ZrV_{1.8}Pd_{0.2}$  retained 80% of the original amount of hydrogen absorbed, which is consistent with the results of the first-principles calculations. Pd maintains the original hydrogen absorption performance to a greater extent than the Hf-doped and undoped surfaces and has the strongest resistance to poisoning. Table 4 indicates that Pd doping boosts the adsorption energy of five of the seven oxygen atom adsorption sites, and it optimizes the amount of hydrogen absorbed after poisoning to a theoretical value of 71%, which is close to the experimental result of 76%. The introduction of Pd and Hf destabilizes the oxygen atom stable adsorption sites, hinders O-V stable bonding, and enhances the total energy of the system, thereby optimizing the anti-poisoning properties relative to the  $ZrV_2$  alloy.

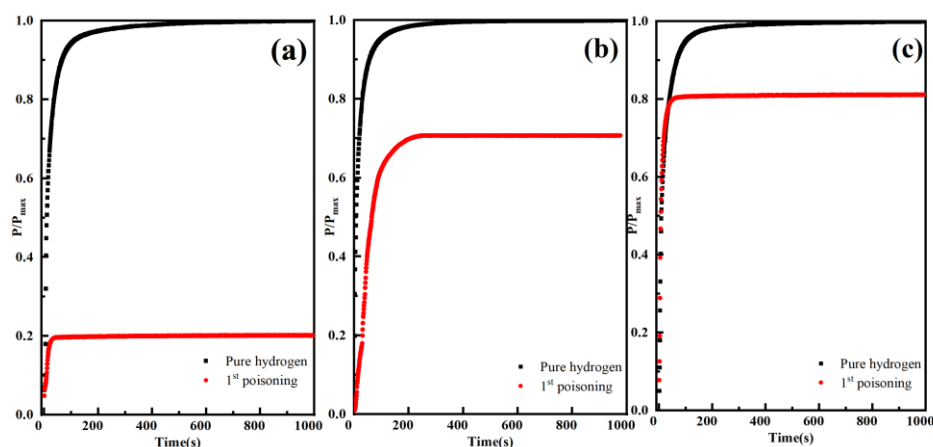


**Fig. 12** Hydrogen-adsorption kinetics in hydrogen–oxygen mixtures of Zr-V-M (M = Hf, Pd) alloys in 0.5 vol%  $O_2$  at room temperature: (a)  $ZrV_2$  alloy, (b)  $ZrVHf$  alloy, (c)  $ZrVPd$  alloy

## 5 Conclusions

In conclusion, this study investigated the effect of doping elements Hf, Pd, and Ti on the anti-poisoning properties of the  $ZrV_2$  alloy using first-principles calculations and experiments. The adsorption behavior was investigated on the most stable surface, (100) of  $ZrV_2$ , using first-principles calculations, which revealed that the preferential adsorption sites for oxygen atoms are bridge sites. The adsorption behavior of oxygen atoms on the bridge sites of the three doped surfaces was studied. The results indicated that the Pd-doped  $ZrV_2$  alloy surface could not adsorb  $O_2$ , and the Hf-doped surface

had an adsorption energy of -1.10 eV; thus, Pd exhibited a good anti-poisoning effect, and Hf was second best. Analysis of the differential charge density and DOS showed that the interaction of the Pd- and Hf-doped atoms with oxygen atoms was reduced, which led to a decrease in the binding force of the oxygen atoms. Based on the results of first-principles calculations, the kinetic behavior of the hydrogen absorption of  $\text{ZrV}_2$ ,  $\text{Zr}_{0.9}\text{Hf}_{0.1}\text{V}_2$ , and  $\text{ZrV}_{1.8}\text{Pd}_{0.2}$  was studied in a hydrogen–oxygen mixture of 0.5 vol%  $\text{O}_2$  at room temperature. The results of the poisoning experiments showed that the hydrogen-absorption values of  $\text{ZrV}_2$ ,  $\text{Zr}_{0.9}\text{Hf}_{0.1}\text{V}_2$ , and  $\text{ZrV}_{1.8}\text{Pd}_{0.2}$  decreased to 19%, 69%, and 80% of their original amounts, respectively.

### **CRedit authorship contribution statement**

**Shuang Yang:** Conceptualization, Methodology, Investigation, Writing – original draft. **Runjie Fang:** Conceptualization, Methodology, Writing – review and editing. **Guo Yang:** Conceptualization, Methodology, Writing – review and editing, Supervision, Funding acquisition. **Lijun Lv:** Writing – review and editing, Supervision, Software. **Xingbo Han:** Conceptualization, Methodology, Writing – review and editing, Supervision, Funding acquisition, Software. **Wei Liu:** Writing –review and editing, Supervision. **Xiujie He:** Writing – review and editing, Supervision. **Pengfei Zhu:** Writing – review and editing, Supervision.

### **Declaration of Competing Interest**

The authors declare that they have no known competing financial interests or personal relationships that may have influenced the work reported in this study.

### **Acknowledgments**

We gratefully acknowledge financial support from the Youth Innovation Promotion Association, Chinese Academy of Science (Grant No. 2019263) and the National Natural Science Foundation of China (No. 12105355).

### **References**

- [1] S.J. Davis, K. Caldeira, H.D. Matthews, Future  $\text{CO}_2$  Emissions and Climate Change from Existing Energy Infrastructure. *Science*. 329, 1330–1333 (2010). <https://doi.org/10.1126/science.1188566>
- [2] G. Principi, F. Agresti, A. Maddalena et al., The problem of solid state hydrogen storage. *Energy*. 34, 2087–2091 (2009). <https://doi.org/10.1016/j.energy.2008.08.027>

- [3] W. Zhang, Y. Hu, L. Ma et al., Progress and Perspective of Electrocatalytic CO<sub>2</sub> Reduction for Renewable Carbonaceous Fuels and Chemicals. *Adv. Sci.* 5, 700275 (2017). <https://doi.org/10.1002/advs.201700275>
- [4] X.Y. Jiang, H.J. Lu, Y.S. Chen et al., Numerical and experimental investigation of a new conceptual fluoride salt freeze valve for thorium-based molten salt reactor. *Nucl. Sci. Tech.* 31, 16 (2020). <https://doi.org/10.1007/s41365-020-0729-5>
- [5] D. Carpenter, M. Ames, G. Zheng et al., Tritium Production and Partitioning from the Irradiation of Lithium-Beryllium Fluoride Salt. *Fusion Sci. Technol.* 71, 549–554 (2017). <https://doi.org/10.1080/15361055.2017.1291040>
- [6] E. Tsitrone, B. Pégourié, Y. Marandet et al., Multi machine scaling of fuel retention in 4 carbon dominated tokamaks. *J. Nucl. Mater.* 415, S735–S739 (2011). <https://doi.org/10.1016/j.jnucmat.2011.01.132>
- [7] T. Tanabe, Tritium fuel cycle in ITER and DEMO: Issues in handling large amount of fuel. *J. Nucl. Mater.* 438, S19–S26 (2013). <https://doi.org/10.1016/j.jnucmat.2013.01.284>
- [8] T.P. Yadav, R.R. Shahi, O.N. Srivastava, Synthesis, characterization and hydrogen storage behaviour of AB<sub>2</sub> (ZrFe<sub>2</sub>, Zr(Fe<sub>0.75</sub>V<sub>0.25</sub>)<sub>2</sub>, Zr(Fe<sub>0.5</sub>V<sub>0.5</sub>)<sub>2</sub> type materials. *Int. J. Hydrog. Energy.* 37, 3689–3696 (2012). <https://doi.org/10.1016/j.ijhydene.2011.04.210>
- [9] A. Jain, R.K. Jain, G. Agarwal et al., Crystal structure, hydrogen absorption and thermodynamics of Zr<sub>1-x</sub>Co<sub>x</sub>Fe<sub>2</sub> alloys. *J. Alloys Compd.* 438, 106–109 (2007). <https://doi.org/10.1016/j.jallcom.2006.08.007>
- [10] P. Chen, M. Zhu, Recent progress in hydrogen storage. *Mater. Today.* 11, 36–43 (2008). [https://doi.org/10.1016/S1369-7021\(08\)70251-7](https://doi.org/10.1016/S1369-7021(08)70251-7)
- [11] J. B von Colbe, J.-R. Ares, J. Barale et al., Application of hydrides in hydrogen storage and compression: Achievements, outlook and perspectives. *Int. J. Hydrog. Energy.* 44, 7780–7808 (2019). <https://doi.org/10.1016/j.ijhydene.2019.01.104>
- [12] Y. Zhang, J. Li, T. Zhang et al., Hydrogen storage properties of non-stoichiometric Zr<sub>0.9</sub>TiV<sub>2</sub> melt-spun ribbons. *Energy.* 114, 1147–1154 (2016). <https://doi.org/10.1016/j.energy.2016.08.085>
- [13] S. Kumar, G.P. Tiwari, S. Sonak et al., High performance FeTi – 3.1 mass % V alloy for on board hydrogen storage solution. *Energy.* 75, 520–524 (2014). <https://doi.org/10.1016/j.energy.2014.08.011>
- [14] T. Wu, X. Xue, T. Zhang et al., Role of Ni addition on hydrogen storage characteristics of ZrV<sub>2</sub> Laves phase compounds. *Int. J. Hydrog. Energy.* 41, 10391–10404 (2016). <https://doi.org/10.1016/j.ijhydene.2014.10.023>
- [15] D. Shaltiel, I. Jacob, D. Davidov, Hydrogen absorption and desorption properties of AB<sub>2</sub> laves-phase pseudobinary compounds. *J. Common Met.* 53, 117–131 (1977). [https://doi.org/10.1016/0022-5088\(77\)90162-X](https://doi.org/10.1016/0022-5088(77)90162-X)
- [16] T.B. Zhang, X.W. Yang, J.S. Li et al., On the poisoning effect of O<sub>2</sub> and N<sub>2</sub> for the Zr<sub>0.9</sub>Ti<sub>0.1</sub>V<sub>2</sub> hydrogen storage alloy. *J. Power Sources.* 202, 217–224 (2012). <https://doi.org/10.1016/j.jpowsour.2011.12.002>
- [17] Y. Zhang, J. Li, T. Zhang et al., Hydrogen absorption properties of a non-stoichiometric Zr-based Laves alloy against gaseous impurities. *Int. J. Hydrog. Energy.* 42, 10109–10116 (2017). <https://doi.org/10.1016/j.ijhydene.2017.02.040>
- [18] F. Sun, M. Yan, X. Liu et al., Effect of N<sub>2</sub>, CH<sub>4</sub> and O<sub>2</sub> on hydrogen storage performance of

- 2LiNH<sub>2</sub> + MgH<sub>2</sub> system. *Int. J. Hydrog. Energy*. 40, 6173–6179 (2015). <https://doi.org/10.1016/j.ijhydene.2015.03.084>
- [19] T. Zhang, Y. Zhang, M. Zhang et al., Hydrogen absorption behavior of Zr-based getter materials with Pd–Ag coating against gaseous impurities. *Int. J. Hydrog. Energy*. 41, 14778–14787 (2016). <https://doi.org/10.1016/j.ijhydene.2016.06.073>
- [20] F. Wang, R. Li, C. Ding et al., Effect of catalytic Pd coating on the hydrogen storage performances of ZrCo alloy by electroless plating method. *Int. J. Hydrog. Energy*. 42, 11510–11522 (2017). <https://doi.org/10.1016/j.ijhydene.2017.03.134>
- [21] K. Zhang, S.K. Gade, J.D. Way, Effects of heat treatment in air on hydrogen sorption over Pd–Ag and Pd–Au membrane surfaces. *J. Membr. Sci.* 403–404, 78–83 (2012). <https://doi.org/10.1016/j.memsci.2012.02.025>
- [22] T. Wu, X. Xue, T. Zhang et al., Poisoning effect of oxygen on hydrogenation performance of a Zr–V–Ni Laves phase alloy. *Int. J. Hydrog. Energy*. 41, 19114–19122 (2016). <https://doi.org/10.1016/j.ijhydene.2016.09.019>
- [23] G. Kresse, J. Furthmüller, Efficiency of ab-initio total energy calculations for metals and semiconductors using a plane-wave basis set. *Comput. Mater. Sci.* 6, 15–50 (1996). [https://doi.org/10.1016/0927-0256\(96\)00008-0](https://doi.org/10.1016/0927-0256(96)00008-0)
- [24] G. Kresse, J. Hafner, Ab initio molecular dynamics for liquid metals. *Phys. Rev. B*. 47, 558–561 (1993). <https://doi.org/10.1103/PhysRevB.47.558>
- [25] J.P. Perdew, K. Burke, M. Ernzerhof, Generalized Gradient Approximation Made Simple. *Phys. Rev. Lett.* 77, 3865–3868 (1996). <https://doi.org/10.1103/PhysRevLett.77.3865>
- [26] H.J. Monkhorst, J.D. Pack, Special points for Brillouin-zone integrations. *Phys. Rev. B*. 13, 5188–5192 (1976). <https://doi.org/10.1103/PhysRevB.13.5188>
- [27] A. Jain, S.P. Ong, G. Hautier et al., Commentary: The Materials Project: A materials genome approach to accelerating materials innovation. *APL Mater.* 1, 011002 (2013). <https://doi.org/10.1063/1.4812323>
- [28] L. Zhu, J. Wang, C. Dong et al., Understanding the surface adsorption and oxidation of cubic Cr<sub>0.5</sub>Al<sub>0.5</sub>N by first-principles calculations. *Comput. Mater. Sci.* 196, 110518 (2021). <https://doi.org/10.1016/j.commatsci.2021.110518>
- [29] H. Cheng, X. Deng, S. Li et al., Design of PC based high pressure hydrogen absorption/desorption apparatus. *Int. J. Hydrog. Energy*. 32, 3046–3053 (2007). <https://doi.org/10.1016/j.ijhydene.2007.01.010>
- [30] K. Zhang, F. Wang, X. Zeng et al., First-principles investigation on the role of interstitial site preference on the hydrogen-induced disproportionation of ZrCo and its doped alloys. *Int. J. Hydrog. Energy* 45, 9877–9891 (2020). <https://doi.org/10.1016/j.ijhydene.2020.01.183>
- [31] T.B. Zhang, X.F. Wang, R. Hu et al., Hydrogen absorption properties of Zr(V<sub>1-x</sub>Fe<sub>x</sub>)<sub>2</sub> intermetallic compounds. *Int. J. Hydrog. Energy*. 37, 2328–2335 (2012). <https://doi.org/10.1016/j.ijhydene.2011.10.089>
- [32] Y.L. Zhang, J.S. Li, T.B. Zhang et al., Microstructure and hydrogen storage properties of non-stoichiometric Zr–Ti–V Laves phase alloys. *Int. J. Hydrog. Energy*. 38, 14675–14684 (2013). <https://doi.org/10.1016/j.ijhydene.2013.09.040>
- [33] M. Zhang, R. Hu, T. Zhang et al., Hydrogenation properties of Pd-coated Zr-based Laves phase compounds. *Vacuum*. 109, 191–196 (2014). <https://doi.org/10.1016/j.vacuum.2014.07.025>
- [34] D. Babai, M. Bereznitsky, D. Mogilyanski et al., Hydrogen sorption behavior of some Pd-

containing compounds. J. Alloys Compd. 750, 206–212 (2018).  
<https://doi.org/10.1016/j.jallcom.2018.03.312>